Lab on a Chip

PAPER

View Article Online
View Journal

Cite this: DOI: 10.1039/d6lc00071a

Nanomembrane-based microfluidic platform with embedded electrical pressure transducer for on-chip nanoparticle quantification

Zachary Morris,[ab] Juliana Chawich,[a] Owen Perreault,[a] Simon Chewchuk,[a] Kate Gragg,[a] Vincent Tabard-Cossa,[ab] James L. McGrath[c] and Michel Godin*[ab]

Accurate quantification of nanoparticle concentration is important in a host of fields, particularly in nanomedicine, electronics, and catalysis. Microfluidic systems present an opportunity to develop low-cost tests for nanoparticle quantification but often suffer technical challenges related to small sample volumes and optical interference from materials used to construct the device. Here we introduce a microfluidic device that integrates an ultrathin silicon nitride nanoporous membrane (nanomembrane) with an on-chip pressure transducer, designed to precisely quantify nanoparticle concentrations within a microfluidic device using an electrical readout for quantification. As nanoparticles are captured by the membrane under pressure-driven flow, the pressure differential across it changes and is measured by an on-chip transducer. The pressure transducer utilizes a thin PDMS membrane that deflects under pressure to change the cross-section and ionic flow resistance of an adjacent channel. This enables the determination of nanoparticle concentration by analysis of the kinetics of trans-membrane pressure changes relative to particle blockage of the nanomembrane. We also propose a statistical model of partial blockage and particle caking in nanoporous membranes, which accounts for distributions in pore and particle sizes. This model provides a more detailed understanding of nanoparticle filtration behavior and the kinetics of nanopore blocking, enabling accurate concentration determination. Experimental validation of the model on the data acquired by the microfluidic device demonstrates a lower limit of detection on the order of 10^8 particles per mL, offering a versatile, non-optical approach for the *in situ* quantification of nanoparticles in a microfluidic device.

Received 23rd January 2026,
Accepted 19th April 2026

DOI: 10.1039/d6lc00071a

rsc.li/loc

1. Introduction

With recent advances in materials science and chemistry, nanoparticles have been synthesized in a variety of shapes and sizes with remarkable uniformity.[1,2] More importantly, these nanomaterials have emerged as a new generation of functional building blocks beyond conventional chemicals, and are being incorporated in a variety of agents and devices, enabling exciting opportunities in electronics, photonics, energy, catalysis, and medicine.[3–5] In most applications, knowledge of the nanoparticle concentration in suspension is essential. While nanoparticle quantification in bulk solutions (μL–mL) is well served by optical and particle-counting methods,[6] quantifying nanoparticle concentration inside microfluidic devices (nL–μL) remains a critical unmet need.

At the macroscale, optical methods such as UV-vis spectroscopy,[7] turbidimetry,[8] and dynamic light scattering (DLS)[9] are among the more commonly used techniques to quantify the concentration of nanoparticles in solution. These approaches involve measuring the intensity of light upon absorption or scattering by a population of nanoparticles. However, they rely on knowledge of the extinction/scattering coefficient or employing a reference sample with a known concentration. Flow cytometry is one of the most commonly used techniques for detecting and quantifying particle concentrations, offering high sensitivity, precision, and rapid data acquisition, making it suitable for high-throughput analysis.[10] However, flow cytometry has some limitations, including high costs for equipment, maintenance and reagents. Furthermore, the need for skilled operators, and challenges with analyzing data generated from submicron particles or those with low refractive indices also complicate quantification, especially within a microfluidic device where low sample volume, optical interference, and short optical path lengths becomes a significant challenge.[11] Additionally, sample preparation requirements, such as labeling with fluorescent

[a] Department of Physics, University of Ottawa, 150 Louis-Pasteur, Ottawa, Ontario, Canada K1N 6N5. E-mail: michel.godin@uottawa.ca
[b] Ottawa-Carleton Institute for Biomedical Engineering, Ottawa, Ontario, Canada
[c] Department of Biomedical Engineering, University of Rochester, Rochester, NY, USA

dyes, can introduce variability and complexity to the process. Fluorescent labeling is especially ineffective in microfluidic systems as the fluorescence output is determined by the number of particles that have been labeled, which presents a challenge at low concentrations and in small sample volumes. Laser-induced breakdown spectroscopy is another method that relies on measuring the plasma generation from nanoparticles in a suspension.[12] It has a wide application for a variety of particles of different sizes, but a continuous wave laser system is required to ensure breakdown of nanoparticles in an aerosolized sample. Resistive-pulsed sensing,[13] single particle inductively coupled plasma-mass spectrometry (spICP-MS),[14] and light scattering particle counter provide concentration information based on the signal pulses from a sensor and a standard reference sample is usually required for calibration, unless sample volume and nanoparticle detection efficiency can be accurately determined. Lastly, while microscopy techniques enable direct visualization of nanoparticles on a surface, it is critical to ensure unbiased counting as the number of nanoparticles in one image may not represent the overall density of nanoparticles in solution.[15]

Nanofabricated porous membranes have shown great potential for the capture and size-selective analysis of nanoparticles.[16,17] These membranes, characterized by their nanoscale pore sizes, are particularly useful in flux filtration and particle capture, enabling precise control over the separation of various components in a mixture.[18] Ultrathin nanoporous silicon nitride (NPN) membranes have particular advantages for membrane-based ultrafiltration of solutions in microfluidic settings due to the tunable, macromolecular scale of both the pore sizes and thickness, the high pore density ($>10^{10}$ pores per cm^2), the chemically inert nature of silicon nitride, and the optical clarity of the membranes.[18–20] The exceptional hydraulic permeability of NPN enables microfluidic flows to operate under manageable pressures, overcoming a major limitation of dramatically increased pressure requirements[21] when incorporating porous media into microfluidic channels.

To enable the nanomembrane's use as *in situ* reporters of particle concentrations, deterministic models of pore blockage during pressure-driven particle capture are needed. Membrane fouling produces non-linear flow and pressure responses, as each capture event eliminates a path through the membrane, alters the local flow field, and reduces the overall hydraulic permeability.[22,23] Fortunately, these complex mechanics can be interpreted from the well-established fluid mechanics of pore fouling during porous filtration. The membrane science literature teaches that kinetics are influenced by multiple mechanisms, such as pore narrowing, complete pore blockage, and particle caking.[24] While traditional models of membrane filtration typically treat the membrane as a uniform permeable medium, NPN has the additional challenge of variations in pore sizes. A mathematical model specifically tailored to account for the unique properties of the microfluidic system is required to provide insight to the mechanisms of nanomembrane fouling as well as produce accurate predictions of sample concentration.

Here, we present a bespoke microfluidic device that integrates an NPN membrane with an on-chip pressure transducer, tailored for electrically quantifying the concentration of nanoparticles in a microfluidic volume. A sample containing nanoparticles is introduced into the microfluidic device using pressure-driven flow. The nanoparticles are captured by the integrated NPN membrane. Upon nanoparticle capture, the fluidic resistance of the NPN increases, provoking predictable changes in pressure within the microchannels. These intra-microchannel pressures are monitored using the custom on-chip pressure transducer. Relying on concepts from the field of membrane filtration science, tracking the kinetics of these pressure changes enables the determination of nanoparticle concentration. We show that the kinetics of nanoparticle capture by the embedded NPN is dominated by two processes: initial nanopore blockage and subsequent nanoparticle caking on the NPN surface. We also developed a computational (or *in silico*) model that accounts for these two mechanisms to predict the kinetics of the measured pressure changes within the device upon nanoparticle capture, providing an ability to quantify the sample's nanoparticle concentration in the ultra-low 800 fM to 80 pM range of concentrations. This microfluidic platform offers a complementary analytical technology capable of sub-picomolar nanoparticle concentration quantification.

2. Results and discussion

2.1 Device for nanoparticle capture and detection

The principle of the device operation is as follows: a sample containing nanoparticles is introduced into a microchannel that leads to an embedded NPN membrane. While nanoparticles are captured by the NPN, fluid continues to flow through the partially blocked membrane into another microchannel below the NPN (Fig. 1).

Under the influence of pressure-driven flow and upon the introduction of a nanoparticle-containing sample, the pressure immediately below the NPN membrane varies as a function of the number of particles captured.[25] These pressure changes are monitored using an integrated microfluidic pressure transducer. If the system is thought of as an analogous electric circuit,[26] the principle used to measure the resistance at the NPN is that of the voltage divider.[27] Placing the transducer pre *vs.* post NPN determines the direction of the measured pressure change as the NPN is blocked. Higher sensitivity will be achieved in whichever section of the channel has higher resistance. A fluidic design with higher resistance was placed post-NPN for simplicity of fabrication and operation compared to placing it pre-NPN. This ensures that the fluidic path pre-NPN could be kept short to avoid dead volume and particle settling while the post-NPN fluidic path could be lengthened to increase hydrodynamic resistance.

The transducer is composed of a thin (10–15 μm) polydimethylsiloxane (PDMS) membrane. When the intra-

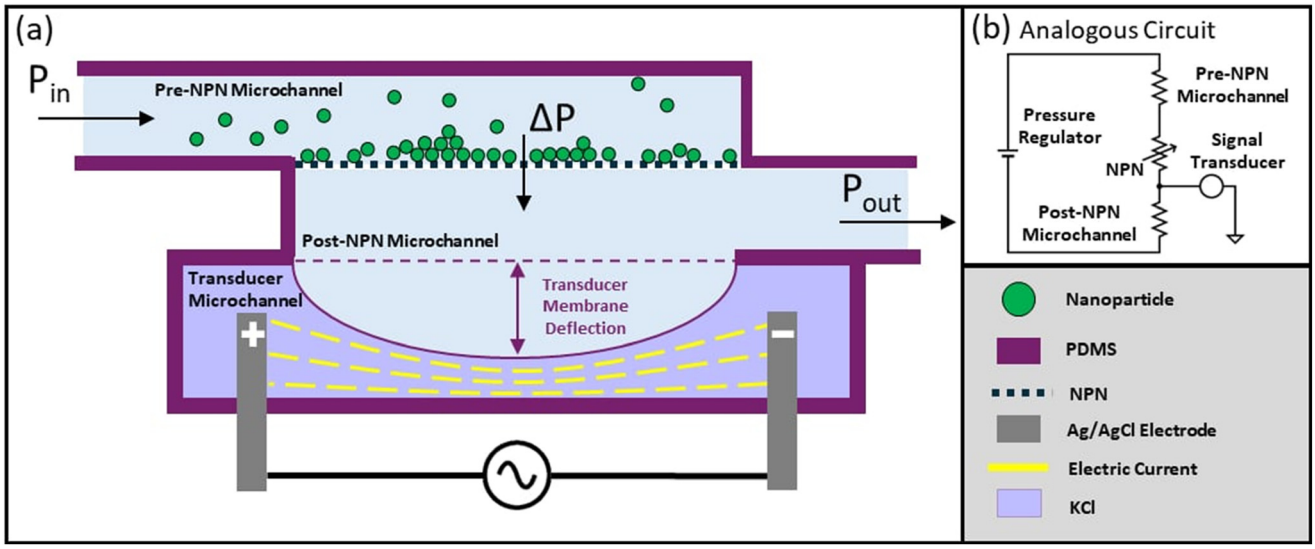

Fig. 1 Microfluidic device overview: (a) cross-sectional view of microfluidic device. As a nanoparticle-containing sample is passed through the NPN, the membrane's 60 nm pores become gradually blocked by the 90 nm particles, which results in a change in the hydrodynamic resistance. As the flow resistance increases a subsequent change in the pressure gradient across the NPN membrane will occur. As the pressure gradient in the post-NPN microchannel changes, a thin PDMS membrane will deflect into the transducer microchannel (TC), this will change the cross-sectional area, and by extension the ionic resistance within the TC. The ionic resistance of the TC is monitored as a function of time using a pair of Ag/AgCl electrodes in order to track pressure changes post NPN. (b) Analogous electric circuit diagram of the microfluidic device. The device can be represented as a simple voltage divider circuit. The pre and post NPN microchannels are hydrodynamically analogous to resistors of constant value in an electric circuit. The NPN can be represented as a variable resistor that increases resistance as it becomes blocked by the nanoparticles. The signal transducer provides insight into the resistivity of the NPN.

channel pressure below the NPN changes, the PDMS membrane deflects into a microfluidic transducer channel (TC) filled with an electrolyte solution (0.1 molar potassium chloride). The TC is kept at a constant pressure (6.9 kPa), causing all of the PDMS membrane deflection to be due to changes of pressure within the post-NPN microchannel. This deflection changes the cross-section of the transducer microchannel, which in turn changes the ionic resistance.[28,29] Variations in the ionic current are monitored using a pair of electrodes to track the change in trans-membrane pressure during testing. The deflection of the pressure transducer's PDMS membrane can be visualized by incorporating coloured solutions into the TC, as shown in Fig. 2a and b. As pressure increases in the post-NPN microchannel, the red fluid in the TC is displaced by the deflected PDMS transducer membrane, which causes the fluid color to appear lighter.

2.2 Pressure transducer calibration

The integrated pressure transducer was calibrated by measuring the ionic current in the TC as a function of trans-membrane pressures. The TC was filled with 0.1 M KCl solution, and a pair of Ag/AgCl electrodes placed in the TC was supplied with an AC signal at 28 mV peak-to-peak voltage. An AC signal was chosen to extend the working life of the electrodes as surface degradation occurred quickly under DC conditions and caused the baseline signal to consistently drift. The current between the electrodes was measured and sent to a current-to-voltage amplifier. The amplified voltage (representative of the current) was sent to a lock-in amplifier to track changes in ionic current. The NPN channels and TC were all initially pressurized to 1 psi (6.9 kPa) *via* the use of digital pressure regulators (SMC ITV1011-311N). Pressure in the NPN channels was increased in increments of 0.5 psi (3.45 kPa) while the TC pressure remained unchanged and the system was allowed 30 s to equilibrate. The mean pressure transducer signal was recorded over 15 s at each pressure and error bars represent the standard deviation of conductance during the sampling period (Fig. 2c). Linear regression analysis was performed on the relationship between signal amplitude and pressure differential between the TC and post-NPN channel to determine system sensitivity.

Within a range of 0–96.5 kPa, the system demonstrated a linear response to pressure differential. The sensitivity of the transducer was determined to be −26 mV kPa^{-1} (Fig. 2c). The limit of detection (LOD) was calculated to be 0.6 kPa or 0.6% full scale. When the pressure differential between the post-NPN microchannel and TC exceeds 96.5 kPa, the system is expected to experience a non-linear voltage response, as the transducer's PDMS membrane completely collapses the TC.[30] Because the Young's modulus of PDMS is thickness dependent for membranes thinner than 200 μm,[31] thinner membranes are expected to lead to higher sensitivity to pressure changes, at the cost of a lower dynamic range. However, we avoided using thinner PDMS membranes to prevent micro-tears in the PDMS. The transducer's linear response and high dynamic range makes it suitable for measuring NPN blockage events within the proposed microfluidic device.

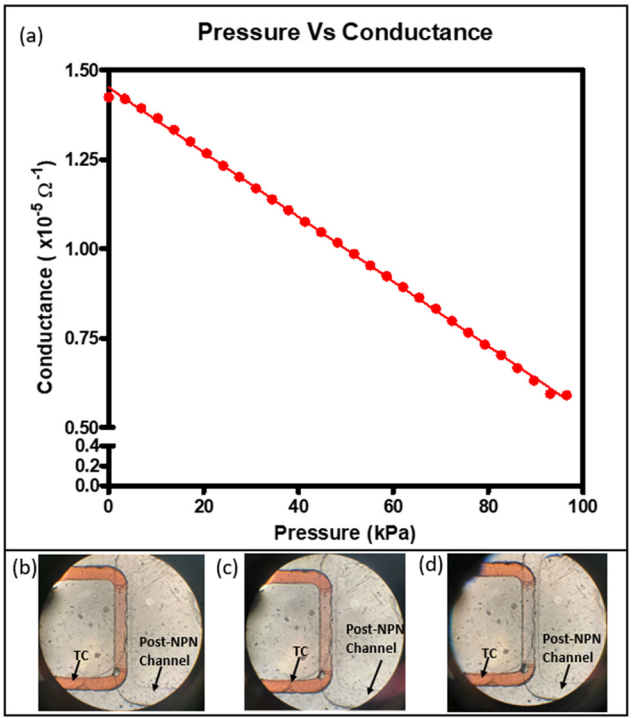

Fig. 2 Transducer calibration. (a) Measured transducer conductance response to change in pressure differential across the PDMS membrane. Data points follow a linear trend (R^2 = 0.999) visual demonstration of the PDMS membrane deflection into the TC at a pressure differential between the post-NPN microchannel [clear] and the TC [red] channel of (b) 0 kPa (c) 34.5 kPa and (d) 103.4 kPa. The PDMS membrane's deflection changes the cross-sectional area and in turn the ionic resistance across the TC, which was measured using Ag/AgCl electrodes.

2.3 Particle capture and data extraction

Prior to particle capture, an in-test calibration cycle (ITCC) was used to account for any voltage drift or baseline changes that could occur during an experiment due to electrode degradation or the presence of nanobubbles in the fluidic pathway. In this method, the pressure gradient across the NPN membrane was first set to zero (stopped flow). The pre-NPN and post-NPN channels were then simultaneously brought to a new matched pressure (either 6.9 kPa or 13.8 kPa) to act as calibration points for known pressures. The voltages recorded at these two pressure settings was used for the in-test calibration of the transducer reporting the microchannel pressure immediately downstream of the NPN membrane (see Fig. 1). Following the completion of an ITCC, a pressure gradient is re-established across the NPN membrane to restart trans-membrane sample flow.

During testing, samples spiked with known concentrations of nanoparticles were passed through the microfluidic device. As nanoparticles were captured by the NPN membrane, the electrical signal measured by the transducer was recorded, allowing tracking of the hydrodynamic resistance across the NPN membrane. The first 180 seconds of the experiment consist of an initial water priming phase (using pressure-driven flow) and of an ITCC. At this stage, the initial wetting efficiency of the NPN was determined. We define wetting efficiency as the percentage of pores in the NPN which are fully accessible to sample flow at the start of the experiment. Wetting efficiency was calculated by dividing the expected hydrodynamic resistance of a theoretically ideal and 100% wetted membrane by the measured NPN flow resistance. Determination of the wetting efficiency of the NPN membrane enables its incorporation as an initial parameter within the fitting algorithm, enhancing the accuracy of subsequent particle concentration calculations. Between 180 s and 240 s of the experimental run the nanoparticle sample was loaded into the device. At time t = 240 s, the pre-NPN microchannel was pressurized to 75.8 kPa and the post-NPN microchannel pressure was set to 6.9 kPa to induce sample flow through the NPN, initiating the particle capture process. At set time points throughout the experiment (60 s, 270 s, 360 s, 660 s, 960 s, and 1260 s) ITCCs were performed to ensure reliable pressure measurements. Initial testing was performed using polystyrene nanoparticles with an average particle diameter of 92 ± 9 nm, at a concentration of 4.9 × 10^9 particles per mL (~8 pM). These particles were selected to ensure that all particles were captured by the nanoporous membrane. NPN membranes with a preset pore size of 60 ± 20 nm were acquired from SiMPore Inc. The smallest particles commercially available that would have no particles flow through a pore given the variance in both pore diameters and particle sizes were selected for testing. As expected, particle capture increased the NPN resistance leading to a reduction in post-NPN microchannel pressure (Fig. 3). For ease of interpretation, time points associated with ITCC events were removed. Visible discontinuities in the signal are an

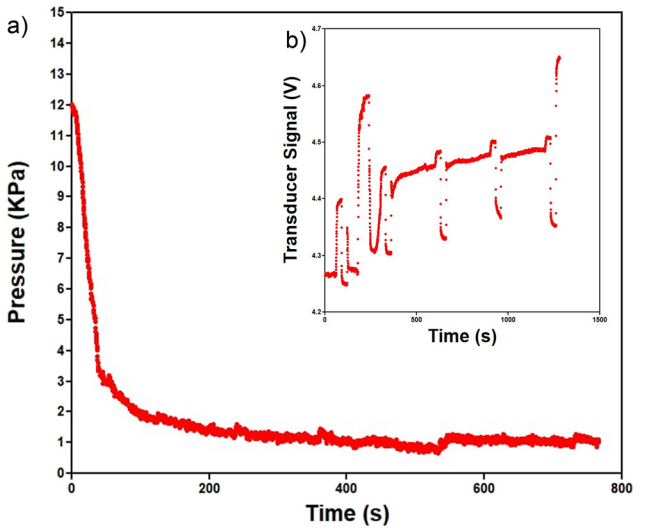

Fig. 3 Pressure response over time for 8 pM polystyrene particle capture. ITCC was performed at several timepoints (60 s, 270 s, 360 s, 660 s, 960 s, and 1260 s). The data was extracted from a test performed with ITCC and a nanoparticle-containing sample. The visible discontinuities are related to these ITCC events. (a) Extracted and processed data (b) raw/unprocessed dataset.

artifact of the removal of these time points and the recalibration that occurs as a result of the ITCCs.

In an ideal scenario, each nanoparticle would fully restrict flow through a given pore. In the case that the membrane becomes saturated with particles, the measured pressure would reduce to 6.9 kPa, equal to the pressure applied to the post-NPN microchannel. However, under real world assay conditions, we expect that a particle will only partially block a given pore and lead to more complex dynamics. To determine the concentration of particles under these conditions, *in silico* modeling of the particle capture process was used to provide insight into the device's response, ultimately providing a method for determination of a sample containing an unknown nanoparticle concentration.

2.4 Computational modeling of pore blocking and particle caking

Factors that affect the NPN blocking dynamics needed to be identified to accurately model the membrane blockage taking place during particle capture in order to provide an accurate particle concentration prediction. Two major modes of particle buildup were considered, contributing to an increase in resistance across the NPN membrane: pore blocking and particle caking (Fig. 4). Due to the slightly irregular shape of the pores and variance in both pore and particle diameters, an imperfect fit of a given nanoparticle to any given pore with some residual fluidic pathways around the particle is common. We therefore defined the term "blockage efficiency" as $\left(1-\frac{\text{Unblocked pore resistance}}{\text{Blocked pore resistance}}\right)\times 100$, corresponding to the percent reduction in flow rate through a given pore when it is partially blocked by a nanoparticle under constant pressure driven flow conditions. It is important to note that blocking efficiency is different than wetting efficiency. While wetting efficiency provides insight into the total number of pores initially available on the NPN membrane for blocking, blockage efficiency estimates the average reduction in flow each individual pore experiences when it becomes blocked by a nanoparticle of a given size. In the case of incomplete blockage, flow is not fully restricted through a given pore when a pressure gradient is applied across the NPN. Additional particles are still driven towards the NPN membrane, although at a reduced flow rate as a function of the given pore blocking efficiency. This phenomenon causes excess nanoparticles to settle on the surface of the NPN and begin stacking on top of each other in a process termed "particle caking" or "cake filtration" (Fig. 4b). As more particles are deposited on the cake layer, the hydrodynamic resistance through the particle caking layer increases.[32,33]

We developed a mathematical model to provide accurate simulations of the system's pressure response kinetics as the particles are captured by the NPN. The core assumption of the model is that the flow of particles through the system exactly follows the fluid flow. In the model, nanopores were considered as cylindrical channels of uniform length L, which allows for the expression of an individual pore's unblocked pore resistance R_i using the Hagen–Poiseuille equation:[34]

$$R_i(x) = \frac{128\mu L}{\pi x^4} \tag{1}$$

where μ is the fluid dynamic viscosity of the sample and x is the pore's characteristic diameter. The fluid flow rate through any given pore is then given by the pressure gradient across the pore divided by the pore resistance. The particle flow rate can then be determined by multiplying the fluid flow by the particle concentration.

As pores become blocked by nanoparticles, the resistance of a given pore increases towards infinity (in the case of perfect pore blockage by a particle). Due to variations in shapes and sizes of both the nanopores and nanoparticles, perfect blockage is rarely achieved and the resistance of a given pore, n, at a given time point t may instead be represented as $R_{p(n,t)}$.

An NPN can be considered as a network of individual nanopores aligned in parallel with one another. The resistance of the NPN, $(R_{NPN(t)})$, at a given time, t, can therefore be expressed as:

$$\frac{1}{R_{NPN(t)}} = \sum_0^n \frac{1}{R_{p(n,t)}} \tag{2}$$

Once the majority of the membranes pores are partially blocked by nanoparticles, the process of particle caking begins.[32,35] In this regime, particles build up on the surface of the NPN membrane, starting with regions next to partially blocked pores and eventually begin to stack atop each other. The caking layer may be thought of as a set of thin capillary channels of increasing length aligned in parallel, through which sample must flow in order to reach the NPN.[25] The resistance provided to the system by particle caking, R_c, can be given as follows:

$$R_c = \frac{\mu h}{kA} \tag{3}$$

where μ is the fluid dynamic viscosity of the sample, h is the height of the caking layer, k is the permeability of the cake, and A is the surface area of the membrane.

The cake height will increase over time as particles continue to be deposited, described by the function $h(t)$. Particles will flow preferentially towards less blocked regions of the NPN. This affects the deposition density and layer permeability of the cake, which in turn affects the added resistance to the system. Lower sample flow occurs towards areas with high hydrodynamic resistance. Decreased flow causes a lower number of particles to settle on the NPN, therefore decreasing the deposition density and increasing layer permeability of the cake.[36] The permeability can then be expressed as a function, $k(z)$, of the vertical position in the caking layer z. Therefore R_c at any given time can instead be represented as:

$$R_c(t) = \int_0^{h(t)} \frac{\mu}{k(z)A}\,dz \tag{4}$$

During the transition from pore blockage to cake filtration, the two mechanisms are interdependent: partial blockage alters

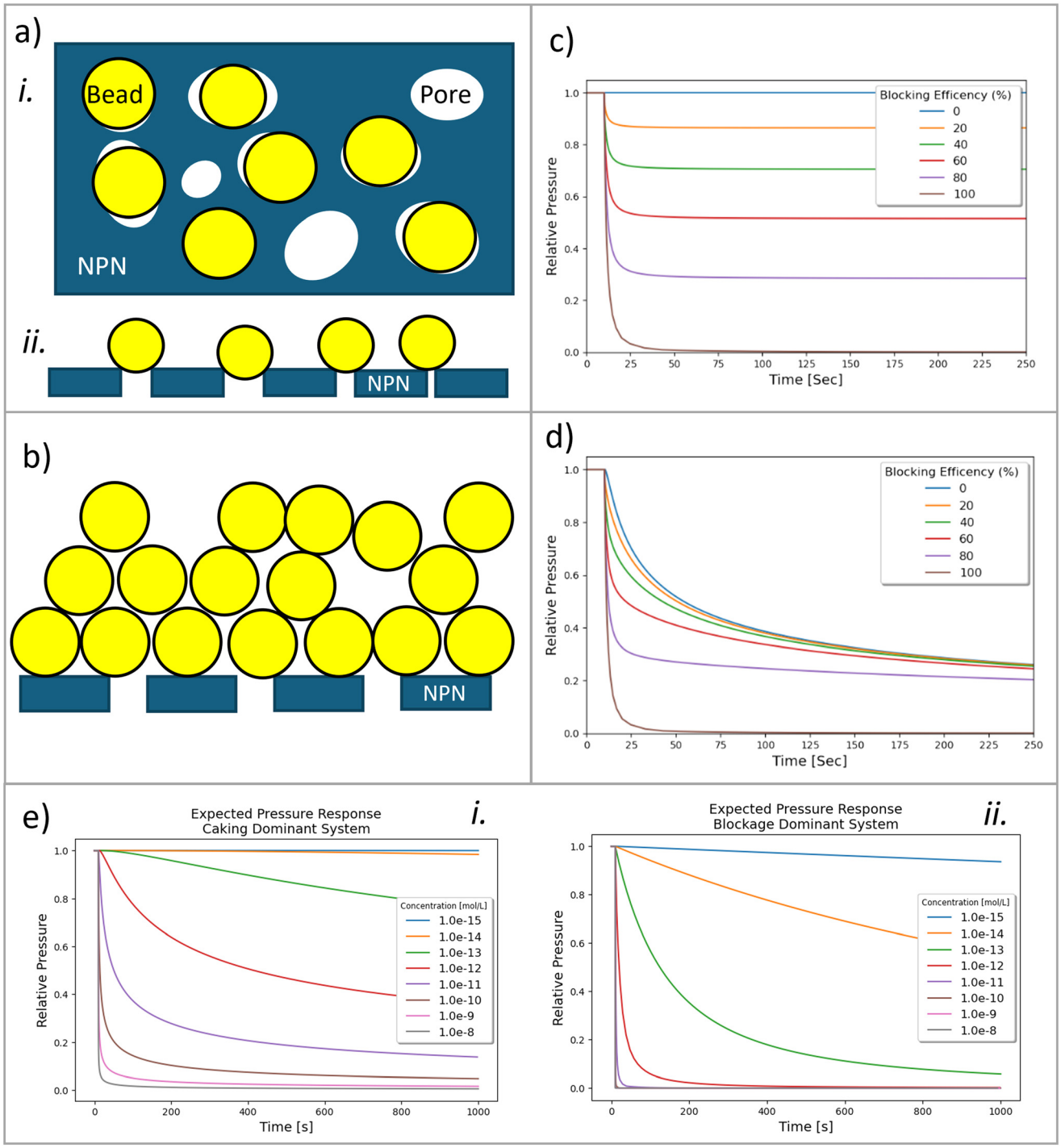

Fig. 4 Methods of membrane nanoparticle capture and effect on measured pressure. (a) Schematic showing pore blockage on an NPN membrane. (i.) Birds-eye view of nanoparticles individually blocking pores on the NPN. (ii.) Cross-sectional view of pore blockage. (b) Cross-sectional view of the nanoparticles depositing on the NPN and stacking in irregular layers to create a "particle caking" effect. As the NPN is blocked with particles, the hydrodynamic resistance at the membrane increases, which contributes to the pressure change at the transducer (diagrams not to scale). (c) Simulation of the nanoparticle efficiency in reducing the trans-pore flow's effect on the measured pressure over time at the transducer. (d) Mixed model simulation of pore blockage and particle caking at different blocking efficiencies on the measured pressure over time at the transducer. (e) Expected detection capabilities for caking dominant system (i) and blockage dominant system (ii) respectively.

local flow patterns that promote cake growth, while the evolving cake layer further modulates pore blockage. A derivation of the system resistance throughout the test is provided in the SI (modeling parameters).

Using the mathematical model described above, the effects of blocking efficiency (Fig. 4c) and particle caking (Fig. 4d) on the pressure response of the device over time were simulated. Our model simulated the transducer's measured pressure after the introduction of a 5×10^9 particle per mL (~8 pM) sample at the NPN membrane. It should be of note that our model considers the physical properties of the system including pore and particle sizes and variability as initial variables for the simulation. These variables are provided by the user and can be modified to fit the unique properties of the system. The model is therefore adaptable to a variety of different membrane and particle parameters. The simulation was considered at various blocking efficiencies over the range of 0–100%. The mixed model of pore blockage and particle caking was utilized to re-simulate the pressure kinetics given the same blocking efficiency values (Fig. 4d). When accounting for only blocking efficiency, a visible difference in pressure plateaus can be observed. Lower observed plateaus are related to increased resistance contributed by more efficiently blocked pores due to the decrease in flow. When a mixed model of pore blockage and caking is considered (Fig. 4d), the difference in plateaus at varying blockage efficiencies is significantly reduced compared to a pore blockage only model (Fig. 4c).

The kinetics of the pressure changes upon particle capture are associated with the sample's particle concentration. When simulating experiments running over 1000 seconds to mirror our experimental time frame, our model predicts the platform's dynamic range (the minimum and maximum detectable particle concentrations). The minimum detectable particle concentration was deemed to be the concentration at which any NPN blockage by particles that may have occurred provides a pressure output indistinguishable from the initial pressure over the given time frame. The maximum detectable particle concentration was deemed to be the concentration at which the complete NPN blockage induced pressure changes that occur so quickly that the kinetics of the system could not be determined due to the limitations caused by the temporal response of PDMS to changes in pressure.[37]

These minimum and maximum detectable concentrations are influenced by various system parameters, such as physical properties of the NPN membrane and/or set pressures pre and post chip. Moreover, the detection capabilities are also influenced by the dominant blockage mode of the system. A caking-dominant system will offer a larger dynamic range but will be less sensitive at low concentrations (Fig. 4e. i). A pore blockage-dominant system will allow for the detection at lower concentrations, but dynamic range will be reduced (Fig. 4e. ii).

Given the uncertainty of the pressure measurements, our simulated data, for our bespoke device, indicates a detectable minimum and maximum particle concentration between approximately 6×10^7 p mL^{-1} and 6×10^{11} p mL^{-1} (100 fM and 1 nM) (Fig. 4e. i) in a caking dominant system, while in a pore blockage dominant system, concentration can be measured between approximately 6×10^6 p mL^{-1} and 6×10^9 p mL^{-1} (10 fM and 10 pM) (Fig. 4e. ii). Experimentally, the dominance of pore blockage and/or caking is difficult to predict. Next, we will show that we can use this model to fit experimental data and the kinetics of particle capture to predict a given sample's particle concentration and the platform's dynamic range.

2.5 Predictive analysis

Having developed a sufficiently descriptive mathematical model for particle blockage of an NPN membrane, Nelder–Mead[38] multivariable optimization was employed to determine the particle concentration and the NPN blocking efficiency. For each iteration in the optimization process, a particle capture event is simulated using the optimizer's prediction for both particle concentration and blocking efficiency. The simulated results are then compared to the experimental data provided to the system, and a coefficient of determination (R^2) value is calculated. The values predicted by the algorithm for the particle concentration and blocking efficiency are those determined to maximize R^2 per the multivariable optimizer. Our custom data acquisition software records individual time points at 4 Hz (every 0.25 s). Initial device testing showed considerable signal drift resulting in altered pressure sensing over time even when no particles had been added. We observed that points farther away from ITCC events had higher uncertainty relative to points closer to the ITCC events. Our algorithm therefore considers time points most proximal to the ITCC event to maximize extrapolation accuracy under all tested conditions. While time points during the initial pressure decline phase of the tests were originally used in the fitting process, accuracy of fit was not significantly improved.

To evaluate the ability of our model to predict particle concentrations accurately and reproducibly, identical replicate experiments were performed four times. Polystyrene nanoparticle (92 ± 9 nm) samples at $(4.9 \pm 0.1) \times 10^9$ particles per mL (8.1 ± 0.2 pM) were introduced to the microfluidic device (inlet pressure: 75.8 kPa, outlet pressure: 6.8 kPa) while the transducer signal was recorded. An initial calibration using an ultrapure water sample was performed and the nanoparticle containing sample was introduced to the system at 240 s. The calibration events (ITCC, as previously described) were included periodically during the test to account for possible signal drift. These ITCC events were also modeled and are visible as sharp discontinuities in the solid line fits (Fig. 5). The time points immediately following the ITCC events were chosen to ensure the highest accuracy of the measured pressure. For each run, the selected points were fed to the analytical model to provide a particle concentration prediction. Nelder–Mead multivariable optimization was used to predict the particle concentration and NPN blocking efficiency that would best fit the pressure kinetics of the experimental results (Fig. 5).

The concentrations predicted by the analytical model for the experimental replicates were 3.6×10^9 particles per mL,

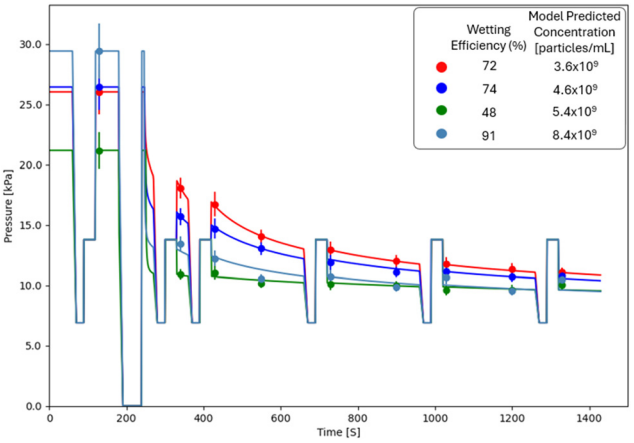

Fig. 5 Effects of NPN wetting efficiency on predictive model: a prepared sample with a concentration of 4.9 × 10^9 particles per mL was passed through 4 separate NPN membranes at varying wetting efficiencies. The predicted concentrations of the runs were 3.6 × 10^9 particles per mL, 4.6 × 10^9 particles per mL, 5.4 × 10^9 particles per mL, and 8.4 × 10^9 particles per mL respectively. Wetting efficiencies of the NPN membranes for each run were determined to be 72%, 74%, 48%, and 91% respectively.

4.6 × 10^9 particles per mL, 5.4 × 10^9 particles per mL, and 8.4 × 10^9 particles per mL respectively. Interestingly, while the same sample concentration was introduced into the device, the capture kinetics are quite different from experiment to experiment. We postulate this is likely due to differences in the NPN wetting efficiency and subsequent particle blocking efficiency, rather than a difference in effective particle concentration. The predictive model was designed to account for differences in initial conditions of the test and still provide a prediction of the sample concentration.

The effects of wetting efficiency on system dynamics are illustrated in Fig. S4. Due to the small pore diameters, the surface tension at the site of the pore is very high, posing difficulty in displacing any air inside the pores and replacing it with liquid. This difficulty in removing excess air results in a decrease in total usable NPN surface and subsequently transmembrane pores. Furthermore, unintended particulate matter in solution, even in ultra-pure water, can block fluidic access to pores decreasing the functional wetting efficiency of the membrane. Although the NPN is treated with piranha solution to increase its hydrophilicity, and an initial wetting of the device is undertaken to maximize the % of pores accessible to flow, a large variance in chip-to-chip wetting efficiencies is still observed. Pending further optimization of membrane wetting, we show that NPN wetting efficiency needs to be accounted for as it affects the initial number of accessible pores and by extension, the initial hydrodynamic resistance of the NPN. This in turn has effects on the pressure response kinetics of the system.

To assess the precision of the analytical model used to predict particle concentration, we employed a bootstrapping approach (S5: error analysis). Briefly, bootstrapping involves random resampling of the experimentally acquired data, fitting a new curve and generating a new concentration prediction for each resample.[39] The resampling and refitting process is repeated 15 000 times, and the predicted concentrations were used to determine frequency and distribution of potential outcomes. The uncertainty determined *via* bootstrapping is representative of the error related to the multivariable fitting algorithm and highlights the variability in the robustness of the fitting algorithm from test to test. Some bootstrapping fits had a low variance in concentration while others were determined to have a wider distribution of predictions. The standard deviation of the bootstraps across experimental runs were 52%, 13%, 10%, and 60% of the mean predicted values. The average uncertainty of the bootstrapping analysis was about ±30% of the mean predicted concentration. The lowest standard deviation values observed were observed during experiments where the NPN membrane wetting efficiency was between 70–75%. Although our model was devised to account for a wide variety of initial variables, further testing is required to determine what role if any wetting efficiency plays in the reproducibility of predicting particle concentration using our multivariable analysis. Our data so far indicates that low wetting efficiency may contribute to higher uncertainty in predictions. We believe this is because of the reduced number of pores available to be blocked. When only a small percentage of pores are available, blocking a single pore contributes to a proportionately larger and more rapid change in pressure. This rapid change in system pressure may exceed the temporal resolution of our system and cause difficulty in producing an accurate and precise prediction. On the other hand, high variability in predicted values at high wetting efficiencies may be due to assumptions made about the physical properties of the membrane. As an example, in several NPN membranes we had tested, we observed the presence of microtears (*i.e.* defects). These defects in the membrane would permit nanoparticles to bypass capture, resulting in an underestimation of particle concentration. To mitigate this, we have implemented more detailed quality control measures in preparing our NPN membrane devices. Conversely, if pore dimensions exceed expected values, the total pore count may decrease while maintaining a high calculated wetting efficiency. Such an issue could increase the magnitude of a pressure drop as a result of any given pore being blocked and may lead to an overestimation of the sample concentration.

Experiments were also performed at three different input particle concentrations (4.9 × 10^8 particles per mL, 4.9 × 10^9 particles per mL, 4.9 × 10^{10} particles per mL or 800 fM, 8 pM, and 80 pM respectively) spanning three orders of magnitude to highlight the method's ability to predict particle concentration within the system's dynamic range. Our model predicted values of 7.33 × 10^8 particles per mL, 7.02 × 10^9 particles per mL, 3.75 × 10^{10} particles per mL or 1.2 pM, 11.7 pM, and 62.3 pM respectively (Fig. 6). Although it may seem as if the final plateau value is heavily correlated with the particle concentration, the entire time course of the test must be considered to properly

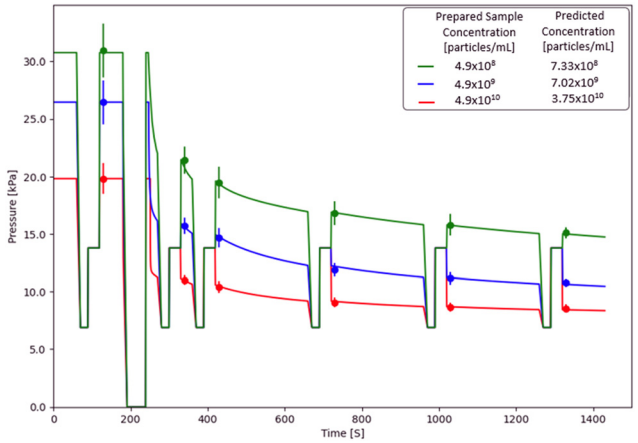

Fig. 6 Pressure measurements over time, visualised with ITCC, for samples tested at concentrations spanning 3 orders of magnitude, for which data fitting was performed (points on the curves). The concentrations determined by the model for samples at 4.9×10^{10} particles per mL (red curve), 4.9×10^{9} particles per mL sample (blue curve) and 4.9×10^{8} particles per mL (green curve), were respectively 3.75×10^{10} particles per mL, 7.02×10^{9} particles per mL and 7.33×10^{8} particles per mL.

determine concentration. While 0.08 pM (5×10^{8} particles per mL) samples were tested, the algorithm was unable to accurately infer sample concentration (data not shown), highlighting a difference between the theoretical and experimentally validated predictive range of the system. At high concentrations, the NPN is blocked too quickly and the predictive algorithm accuracy decreased. At low concentrations, the system pressure changes minimally over time, and the algorithm is equally inaccurate. At this time, the model is only capable of accurately predicting concentrations in the 10^{8}–10^{10} particles per mL range. Further refinement of the predictive algorithm and a device redesign may help in reducing sampling uncertainty and extend the dynamic range of the system.

One technique capable of quantifying such low particle concentration is nanoparticle tracking analysis (NTA).[40] While our technique is marginally less accurate, it operates in a larger dynamic range without increasing the minimum detectable concentration. Multi-angle dynamic light scattering (MADLS)[41] is a commercially available technique capable of quantifying low nanoparticle concentration in solutions. The method we propose here is comparable in both accuracy and dynamic range to that of MADLS. Our proposed technique aims to act as a complementary tool to both NTA and MADLS, providing a secondary, non optical validation method for use within microfluidic systems.

Additional experiments were conducted for concentrations outside of the reported dynamic range. While our system was able to monitor the changes in pressure, the predictive model fitting failed to converge. The physics model and fitting algorithm may be evaluated and adjusted to increase both the accuracy and dynamic range of the predictive model moving forward. Our model currently considers all pores to be perfectly cylindrical and all particles to be perfectly spherical, but in reality, this is not the case. Better characterization of the NPN and the nanoparticles can help improve the simulations and the accuracy of the fit. Due to the disruptive nature of ITCC events on the flow conditions, the number of calibration events have been minimized, as they may contribute to inaccuracies in the predictive analysis. A less disruptive internal calibration cycle would allow for the acquisition of more data points within an experimental run, which in turn would increase the accuracy of the model fitting. Alternatively, investigation into the minimization of signal drift would mitigate requirements for ITCC events. Improving NPN wetting efficiency should additionally enhance pore accessibility, which in turn minimizes initial NPN resistance, ultimately leading to more pronounced pressure variations throughout the test. Matching the density of the suspension solution to the density of the nanoparticles may also reduce predictive error of the system. In a density matched solution, nanoparticles would remain suspended for prolonged periods of time, reducing the likelihood of local changes in sample concentration due to particles settling within the device.

3. Conclusion

In this study, we have investigated the nanoparticle capture and quantification on nanoporous membranes integrated within microfluidic devices, using an on-chip PDMS pressure transducer coupled to an electrical readout. The real-time pressure measurements obtained from the integrated transducer provided valuable insights into the dynamics of pore blockage and caking processes, enabling us to correlate pressure changes with nanoparticle accumulation in the low picomolar to high femtomolar range. We observed that as particle concentration increases, a critical threshold is reached where caking occurs, drastically reducing permeability. The integration of the PDMS pressure transducer facilitated continuous monitoring of pore blockage and caking processes. Our findings reveal that the nanoparticle capture efficiency is significantly influenced by the membrane wetting efficiency. More work is required to reproducibly wet the membrane and allow for maximum capture efficiency. The system's ability to calculate chip wetting efficiency using initial signal readings and the first ITCC event allows it to be used as an initial variable in the simulation process, making the system adaptable to a variety of non-ideal conditions while still providing an accurate prediction of concentration.

This proof-of-concept device paves the way for designing more efficient filtration systems used in various applications, from biomedical devices to environmental monitoring. Future work will focus on exploring the effects of varying particle types and sizes, to explore the effects of different nanoparticle characteristics and operational conditions on capture efficiency and caking dynamics. By enhancing the understanding of these dynamics, advanced microfluidic platforms capable of *in situ* assessments of nanoparticle concentrations can be developed.

4. Materials and methods

4.1 NPN device fabrication

3D printing of microfluidic components. All microfluidic device and assembly components were designed in Onshape[42,43] and exported as STL files for slicing in CHITUBOX (version 1.6.5.), at a layer thickness of 20 μm. The molds, alignment modules and gaskets were 3D-printed with ELEGOO Mars 4 Ultra 3D printer (ELEGOO, China), with a 405 nm light source and 9K monochrome LCD, using ELEGOO ABS-like resin (1.8 s layer exposure time). Once completed, the prints were removed from the build plate and washed in isopropyl alcohol (Sigma Millipore, Canada) for 30 minutes to remove excess uncured resin. The prints were air dried for 30 minutes, then cured using the Intelliray 400 Shuttered UV Flood cure system at 115 mW cm^{-2} power for 30 minutes. Exceptionally, the gaskets were UV cured for only 2 minutes. Following the post-processing, all molds were treated with trichloro(3,3,4,4,5,5,6,6,7,7,8,8,8-tridecafluorooctyl) silane (Millipore Sigma, Canada) to facilitate the PDMS removal.

Resin mold replica with PDMS. Degassed polydimethylsiloxane (PDMS Sylgard 184 kit, Dow Chemical Company) mixtures were prepared at 10 : 1 base to cross linker ratio, then poured onto the 3D-printed resin molds and degassed for 10 minutes. The molds were then placed in an oven at 70 °C for 4 hours. The cured PDMS was subsequently removed from the molds using a scalpel, and holes were punched in the PDMS using biopsy punches to provide fluidic and electrical access to the microchannels (0.75 mm in diameter for fluidic ports, and 1.25 mm in diameter for electrodes). PDMS mixtures for the transducer layer were degassed, then spun at a thickness of ~105 μm, and baked in the oven at 70 °C for 40 minutes.

Chip preparation. The 250 × 2800 μm^2, 100 nm thick NPN membranes supported on 310 μm thick, 6.4 mm × 6.4 mm frame size silicon chips, used in this work, were obtained from SiMPore Inc. (West Henrietta, NY). The membranes have an average pore diameter of ~58.9 nm, a standard deviation of 18 nm and ~16.4% porosity, as determined by electron microscopy. Prior to assembly, the chips were submerged for 15 minutes in piranha solution for cleaning, rinsed with DI water then stored in 50% ethanol solution. Detailed protocol for assembly is provided in SI.

4.2 Nanoparticles quantification experiments

Sample preparation. For the nanoparticle quantification experiments, Polystyrene beads were used as model analytes, because they are monodisperse and exhibit no significant propensity to adsorb to the NPN membrane.[44] The polystyrene beads were purchased from Bangs Laboratories Inc, USA, with an average diameter of 92 nm and a coefficient of variation of 5–10%. The stock solution of 2.45 × 10^{13} particles per mL was diluted to suitable testing concentrations *via* serial dilution in UltraPure distilled water (Invitrogen, USA).

Device priming and testing. Prior to testing, the device was submerged in DI water and placed under vacuum for 1 hour to ensure wetting of the NPN and the microfluidic channels. In order to prime the fluidic testing channels, the system was pressurized (pre-NPN: 10 psi, post-NPN: 0 psi) and DI water was flown to wet the NPN membrane. The transducer channel (TC) was primed with 0.1 M KCl buffered using 20 mM HEPES Buffer (VWR International, China). Sintered Ag/AgCl pellet electrodes of 1 mm diameter (ALA Scientific Instruments Inc., USA), were inserted in the transducer microchannel with careful attention to prevent air bubbles. The electrodes were supplied with an AC current (Stanford Research Systems Model DS345; 50 kHz, 0.0283 Vpp), and the signal was sent to a Keithley 428 Current Amplifier (1000× amplification). The output from the I/V amplifier was sent to a Stanford Research Systems Lock-In Amplifier (Model SR830 DSP, time constant: 10 ms, sensitivity: 500 μV), to determine the peak to peak voltage of the signal, which was sent to a National Instruments PCI-6221 37-pin data acquisition card (DAQ) using a LabVIEW (National Instruments) program custom designed for testing and calibration of the device.

The LabVIEW program sets the regulator's output throughout the test, processes the signal using smoothing and low pass filtering to reduce the system's noise, and records the signal for analysis. During testing, a 10 psi pressure differential is applied across the NPN to push the sample through the membrane, and the transducer microchannel is pressurized to 1 psi. The program additionally includes ITCC "calibration events" at set times throughout the test (60 s, 270 s, 360 s, 660 s, 960 s, 1260 s) to ensure accurate measurement of the pressure, by reducing uncertainty related to noise and electrical baseline shifts that may occur during the test. During these calibration events, the entire testing channel was set to 1 psi for 30s to establish a baseline voltage, then the pressure was changed to 2 psi, and the voltage was measured for 30 s to establish a trend between the measured voltage and pressure. The test was run for 30 minutes to allow for maximal saturation of the NPN with the polystyrene nanoparticles.

Chip regeneration. At the end of each test, the devices were disassembled, and the chips were thoroughly cleaned using piranha solution to dissolve the polystyrene beads, and render the membranes sufficiently hydrophilic for subsequent proper wetting prior to reusing them in further testing.

4.3 Modeling of nanoparticle blockage and caking dynamics

A pore blockage and caking model was implemented in Python 3.11.8,[45] using Jupyter Notebook[46] to simulate the fluid flow and particle capture process. Included in the program are the NumPy[47] library, pyplot module from the matplotlib[48] library, the math[49] library, and the csv[50] library.

The membrane characteristics were provided by the manufacturer to be L = 100 nm, A = 0.7 mm^2, ϕ = 0.104, $\bar{x}$ = 58.9 nm, σ_x = 18 nm, where L is the NPN thickness, A is the NPN surface area, ϕ is NPN porosity, $\bar{x}$ is the average pore diameter, and σ_x is the standard deviation of pore diameters. The manufacturer's given values were implemented in the model, along with the nanoparticles' specifications ($\bar{y}$ = 92

nm, σ_y = 5 nm) where $\bar{y}$ is the average nanoparticle diameter and σ_y is the standard deviation of the nanoparticles' diameter. Given that the nanoparticles sample was prepared in ultrapure water, the physical properties of water at 25 °C (ρ = 997 kg m^{-3}, $\mu = 8.9 \times 10^{-4}$ Pa s)[51] were included.

The inlet and outlet tubing resistances were determined experimentally using a simple flow rate test, where water was flowed through the tubing at multiple set pressures and collected in a sample vial, and the difference in mass of the collection vial before and after the experiment gave a measure of the flowed fluid volume, which was used to determine the flow rate for the set duration. The resistance values were found to be $R_{in} = 6.6 \times 10^{11}$ Pa s m^{-3}, $R_{out} = 8.9 \times 10^{12}$ Pa s m^{-3}.

Fitting of the experimental data was performed using the Nelder–Mead method[52] for optimizing multivariable functions. For a given concentration and blocking efficiency multiplier, the simulation was run and then compared to the experimental data to calculate a coefficient of determination, represented as the function R^2. The Nelder–Mead method minimizes the function, so to maximize R^2, the minimization was performed on the opposite function $-R^2$. When the algorithm converges towards an optimal value, the coefficient of determination should generally be above 0.99. Further details on the modeling parameters are provided in the SI.

Author contributions

M. G. and J. C. designed the experimental study. Z. M. and O. P. developed the device assembly protocols, and performed and analyzed the nanoparticle capture experiments. O. P. designed the pore blockage and caking model. J. C. and Z. M. wrote the first draft. J. L. M. provided NPN material and related expertise. M. G., Z. M., V. T.-C., S. C. and K. G. provided insights and interpretation for the understanding of data. All authors contributed to the revision of the manuscript.

Conflicts of interest

J. L. M. is a co-founder and equity holder of SiMPore Inc which manufactures NPN commercially. All other authors declare they have no competing interests.

Data availability

Data for this article, including raw data sets for membrane blockage experiments presented within the manuscript as well as all code for predictive data analysis and bootstrapping are available on GitHub at https://github.com/zabmorris/Nanoparticle-Capture-and-Quantification.git.

Supplementary information (SI) is available. See DOI: https://doi.org/10.1039/d6lc00071a.

Acknowledgements

The authors would like to thank Josh Miller and SiMPore Inc. for providing technical expertise and NPN membrane materials. We would additionally like to thank Dmytro Lomovtsev for his expertise in 3D printing for microfluidic applications. Thank you to Morteza Safari and Nicholas Soucy for insightful discussions. We acknowledge funding support from the National Institutes of Health (NIH) [1R01EB031581-01] and the Natural Sciences and Engineering Research Council of Canada (NSERC) [RGPIN-2020-05012].

References

1 K. Ma, *et al.*, Using Gradient Magnetic Fields to Control the Size and Uniformity of Iron Oxide Nanoparticles for Magnetic Resonance Imaging, *ACS Appl. Nano Mater.*, 2022, **5**, 7410–7417.
2 S. Lee, Highly uniform silica nanoparticles with finely controlled sizes for enhancement of electro-responsive smart fluids, *J. Ind. Eng. Chem.*, 2019, **77**, 426–431.
3 M. S. Rider, *et al.*, Advances and Prospects in Topological Nanoparticle Photonics, *ACS Photonics*, 2022, **9**, 1483–1499.
4 T. Joseph, *et al.*, Nanoparticles: Taking a Unique Position in Medicine, *Nanomaterials*, 2023, **13**, 574.
5 G. Martínez, *et al.*, Environmental Impact of Nanoparticles' Application as an Emerging Technology: A Review, *Materials*, 2020, **14**, 166.
6 M. M. Modena, B. Rühle, T. P. Burg and S. Wuttke, Nanoparticle Characterization: What to Measure?, *Adv. Mater.*, 2019, **31**, 1901556.
7 T. Hendel, *et al.*, In Situ Determination of Colloidal Gold Concentrations with UV–Vis Spectroscopy: Limitations and Perspectives, *Anal. Chem.*, 2014, **86**, 11115–11124.
8 X. Gao, *et al.*, Lectin-conjugated PEG–PLA nanoparticles: Preparation and brain delivery after intranasal administration, *Biomaterials*, 2006, **27**, 3482–3490.
9 M. Kaszuba, D. McKnight, M. T. Connah, F. K. McNeil-Watson and U. Nobbmann, Measuring sub nanometre sizes using dynamic light scattering, *J. Nanopart. Res.*, 2008, **10**, 823–829.
10 H. Shin, M. Kwak, T. G. Lee and J. Y. Lee, Quantifying the level of nanoparticle uptake in mammalian cells using flow cytometry, *Nanoscale*, 2020, **12**, 15743–15751.
11 P. Zhou, H. He, H. Ma, S. Wang and S. Hu, A Review of Optical Imaging Technologies for Microfluidics, *Micromachines*, 2022, **13**, 274.
12 D. J. Palásti, *et al.*, Detection and characterization of mono- and bimetallic nanoparticles produced by electrical discharge plasma generators using laser-induced breakdown spectroscopy, *Spectrochim. Acta, Part B*, 2023, **209**, 106804.
13 G. R. Willmott, *et al.*, Use of tunable nanopore blockade rates to investigate colloidal dispersions, *J. Phys.: Condens. Matter*, 2010, **22**, 454116.
14 S. Hu, *et al.*, A new strategy for highly sensitive immunoassay based on single-particle mode detection by inductively coupled plasma mass spectrometry, *J. Am. Soc. Mass Spectrom.*, 2009, **20**, 1096–1103.
15 R. M. Lee, L. R. Eisenman, S. Khuon, J. S. Aaron and T.-L. Chew, Believing is seeing – the deceptive influence of bias in quantitative microscopy, *J. Cell Sci.*, 2024, **137**, jcs261567.
16 M. Paul-Tiberiu, S. Richter and C. Hagendorf, Nanoporous membrane filter cascade for size-selective analysis of nano-

and microplastic particles, *Appl. Res.*, 2023, **2**(5), DOI: 10.1002/appl.202200094.
17 K. Lucas, *et al.*, A predictive model of nanoparticle capture on ultrathin nanoporous membranes, *J. Membr. Sci.*, 2021, **633**, 119357.
18 J. P. S. DesOrmeaux, *et al.*, Nanoporous silicon nitride membranes fabricated from porous nanocrystalline silicon templates, *Nanoscale*, 2014, **6**, 10798–10805.
19 K. Hill, *et al.*, Second Generation Nanoporous Silicon Nitride Membranes for High Toxin Clearance and Small Format Hemodialysis, *Adv. Healthcare Mater.*, 2020, **9**, 1900750.
20 C. C. Striemer, T. R. Gaborski, J. L. McGrath and P. M. Fauchet, Charge- and size-based separation of macromolecules using ultrathin silicon membranes, *Nature*, 2007, **445**, 749–753.
21 M. Dehghani, K. Lucas, J. Flax, J. McGrath and T. Gaborski, Tangential flow microfluidics for the capture and release of nanoparticles and extracellular vesicles on conventional and ultrathin membranes, *Adv. Mater. Technol.*, 2019, **4**, 1900539.
22 J. D. Winans, K. J. P. Smith, T. R. Gaborski, J. A. Roussie and J. L. McGrath, Membrane capacity and fouling mechanisms for ultrathin nanomembranes in dead-end filtration, *J. Membr. Sci.*, 2016, **499**, 282–289.
23 K. J. P. Smith, M. May, R. Baltus and J. L. McGrath, A predictive model of separations in dead-end filtration with ultrathin membranes, *Sep. Purif. Technol.*, 2017, **189**, 40–47.
24 C. Orsello, W. Li and C.-C. Ho, A three mechanism model to describe fouling of microfiltration membranes, *J. Membr. Sci.*, 2006, **280**, 856–866, DOI: 10.1016/j.memsci.2006.03.005.
25 E. Iritani, A Review on Modeling of Pore-Blocking Behaviors of Membranes During Pressurized Membrane Filtration, *Drying Technol.*, 2013, **31**, 146–162.
26 Z. Li, C. Liu and J. Sun, Hydraulic–electric analogy for design and operation of microfluidic systems, *Lab Chip*, 2023, **23**, 3311–3327.
27 G. L. Zeng and M. Zeng, Voltage Divider and Current Divider, in *Electric Circuits: A Concise, Conceptual Tutorial*, ed. G. L. Zeng and M. Zeng, Springer International Publishing, Cham, 2021, pp. 43–48, DOI: 10.1007/978-3-030-60515-5_7.
28 C.-Y. Wu, J.-C. Lu, M.-C. Liu and Y.-C. Tung, Integrated electrofluidic circuits: pressure sensing with analog and digital operation functionalities for microfluidics, *Lab Chip*, 2012, **12**, 3943–3951.
29 C.-Y. Wu, W.-H. Liao and Y.-C. Tung, Integrated ionic liquid - based electrofluidic circuits for pressure sensing within polydimethylsiloxane microfluidic systems, *Lab Chip*, 2011, **11**, 1740–1746.
30 K. A. Gopinathan, A. Mishra, B. R. Mutlu, J. F. Edd and M. Toner, A microfluidic transistor for automatic control of liquids, *Nature*, 2023, **622**, 735–741.
31 M. Liu, J. Sun, Y. Sun, C. Bock and Q. Chen, Thickness-dependent mechanical properties of polydimethylsiloxane membranes, *J. Micromech. Microeng.*, 2009, **19**, 035028.
32 P. Sanaei and L. J. Cummings, Membrane filtration with multiple fouling mechanisms, *Phys. Rev. Fluids*, 2019, **4**(12), 124301.
33 E. Dressaire and A. Sauret, Clogging of microfluidic systems, *Soft Matter*, 2017, **13**, 37–48.
34 H. Bruus, *Theoretical Microfluidics*, Oxford University Press, Illustrated edn, 2007.
35 J. D. Winans, K. J. P. Smith, T. R. Gaborski, J. A. Roussie and J. L. McGrath, Membrane capacity and fouling mechanisms for ultrathin nanomembranes in dead-end filtration, *J. Membr. Sci.*, 2016, **499**, 282–289.
36 O. T. Majekodunmi and S. M. Hashmi, Flow dynamics through discontinuous clogs of rigid particles in tapered microchannels, *Sci. Rep.*, 2022, **12**, 22587.
37 P. Panda, K. P. Yuet, D. Dendukuri, T. Alan Hatton and P. S. Doyle, Temporal response of an initially deflected PDMS channel, *New J. Phys.*, 2009, **11**, 115001.
38 M. A. Luersen and R. Le Riche, Globalized Nelder–Mead method for engineering optimization, *Comput. Struct.*, 2004, **82**, 2251–2260.
39 B. Efron and R. Tibshirani, The Bootstrap Method for Assessing Statistical Accuracy, *Behaviormetrika*, 1985, **12**, 1–35.
40 Y. Tian, D. Tian, X. Peng and H. Qiu, Critical parameters to standardize the size and concentration determination of nanomaterials by nanoparticle tracking analysis, *Int. J. Pharm.*, 2024, **656**, 124097.
41 J. Austin, C. Minelli, D. Hamilton, M. Wywijas and H. J. Jones, Nanoparticle number concentration measurements by multi-angle dynamic light scattering, *J. Nanopart. Res.*, 2020, **22**, 108.
42 S. Junk and C. Kuen, Review of Open Source and Freeware CAD Systems for Use with 3D-Printing, *Proc. CIRP*, 2016, **50**, 430–435.
43 E. Moss, *Getting Started with Onshape*, SDC Publications, 4th edn, 2023.
44 J. D. Winans, K. J. P. Smith, T. R. Gaborski, J. A. Roussie and J. L. McGrath, Membrane capacity and fouling mechanisms for ultrathin nanomembranes in dead-end filtration, *J. Membr. Sci.*, 2016, **499**, 282–289.
45 Python Release Python 3.11.8, Python.org, https://www.python.org/downloads/release/python-3118/.
46 Project Jupyter Documentation – Jupyter Documentation 4.1.1 alpha documentation, https://docs.jupyter.org/en/latest/.
47 NumPy documentation – NumPy v2.1 Manual, https://numpy.org/doc/stable/.
48 matplotlib.pyplot – Matplotlib 3.5.3 documentation, https://matplotlib.org/3.5.3/api/_as_gen/matplotlib.pyplot.html.
49 math – Mathematical functions, Python documentation, https://docs.python.org/3/library/math.html.
50 csv – CSV File Reading and Writing, Python documentation, https://docs.python.org/3/library/csv.html.
51 J. C. Crittenden, R. R. Trussell, D. W. Hand, K. J. Howe and G. Tchobanoglous, Appendix C: Physical Properties of Water, in *MWH's Water Treatment: Principles and Design*, 3rd edn, 2012, DOI: 10.1002/9781118131473.app3.
52 J. A. Nelder and R. Mead, A Simplex Method for Function Minimization, *Comput. J.*, 1965, **7**, 308–313.